Vicarious radiometric calibration of a multispectral sensor from an aerial trike applied to precision agriculture

Mónica Herrero-Huerta [a], David Hernández-López [b], Pablo Rodriguez-Gonzalvez [a,*],
Diego González-Aguilera [a], José González-Piqueras [b]

[a] Department of Cartographic and Land Engineering, University of Salamanca, Higher Polytechnic School of Avila, Hornos Caleros 50, 05003 Avila, Spain
[b] Institute for Regional Development (IDR), University of Castilla La Mancha, 02071 Albacete, Spain

ARTICLE INFO

ABSTRACT

This article proposes a vicarious calibration as a radiometric calibration method using an onboard multispectral sensor and a low-cost manned aerial platform, PPG (powered paraglider) trike. The statistical analysis of the errors shows the precision reached with this methodology. The greatest advantage offered by this type of manned platforms is its flexibility of flight, autonomy and payload capacity, allowing multiple sensors to be integrated without constraints to weight and volume. The results were validated at two different heights in order to verify the solution obtained with the method, demonstrating the insignificance of relative atmospheric influence between the aerial platform and ground using this platform according to the radiative transfer model on a clear and sunny day. At the same time, the study aims to develop a new trend for remote sensing that will assists in decision making for the sustainable management of extensive crop areas using low-cost geomatic techniques. As a result of the radiometric calibration process, georeferenced images with different vegetation indices over vineyards are obtained.

© 2014 Elsevier B.V. All rights reserved.

1. Introduction

The possibility of loading multispectral cameras on low-cost manned aerial platforms such as PPG trikes enables highly accurate radiometric studies to be performed. Therefore, it is desirable that the sensor should be subjected a calibration in which the radiometric behavior of each pixel in the different regions of the spectrum is analyzed, using as "ground truth" the radiance obtained on different targets with the calibrated spectroradiometer (Honkavaara et al., 2009). The basis of this behavior lies in the fact that each body has a typical and different pattern of reflected/emitted energy when it is influenced by electromagnetic energy, which distinguishes it from other materials (Chuvieco and Huete, 2009) depending on atmospheric conditions and the sensor characteristics (Biggar et al., 2003).

The main limitation of PPG trikes to make use of methodologies based on quantitative remote sensing is the need to develop radiometric calibration methodologies to obtain validated radiance data. As advantages, PPG trikes are able to acquire higher spatial, spectral and mainly temporal resolution data with a lower associated cost (Hailey, 2005) and, also, the relative atmospheric corrections required for validating the radiance data are likely to

be insignificant on a clear and sunny day. The high spatial resolution data available from conventional platforms, such as satellites and manned aircrafts, is usually limited to a Ground-Sample Distance (GSD) of 50 cm/pixel. Instead, PPG trikes are capable of flying lower than a conventional manned aircraft and therefore acquire images of higher resolution, reaching up to 5–10 cm/pixel. In addition, the ease of flight planning permits better temporal resolution than classic photogrammetric flight planning (Hernandez-Lopez et al., 2013). In satellite systems, temporal resolution is limited by the coverage patterns of the satellite's orbit, involving lengthy periods in the delivery of the results (unfavorable temporal resolution) (Berni et al., 2009). Regarding unmanned aerial systems (UAS), the payload capacity and volume of onboard sensors as well as the limited flight autonomy means that the mapping and monitoring of large surfaces and ground covers are unviable. Last but not least, the progress of microelectronics in the field of navigation equipment (GNSS/IMU-Global Navigation Satellite System/Inertial Measurement Unit) has made it possible to provide these low-cost manned platforms with a quality solution to determine the spatial and angular position of the sensors and consequently their trajectory.

A key factor in the suitability of close-range remote sensing for vegetation analysis (i.e. precision agriculture) is based on the fact that such sensing procedures are non-destructive and non-invasive, providing similar accuracy to destructive field methods (Zhang and Kovacs, 2012). More specifically, the spectral signature

of a given crop is directly related to its phenological, physiological and morphological characteristics, such that any change in the plant will also disturb its reflectance (Lass and Callihan, 1997; Schmidt and Skidmore, 2003). These differences in the intrinsic spectral behavior of each species allow their discrimination and mapping by analysis techniques and digital classification. This is why the spectral signatures of different types of vegetation can be assessed, supported by vegetation indices and the subsequent biophysical magnitudes used in agricultural applications.

The most widely used and most familiar vegetation index is the Normalized Difference Vegetation Index (NDVI) developed by Rouse et al. (1974), which is based on contrasts between maximum absorption in the red spectral region, because of chlorophyll pigments, and maximum reflection in the infrared region, caused by the cell structure of leaves and reflection of the cover due to its structure. Despite its intensive application, in cases of dense covers or those consisting of several layers the NDVI becomes saturated, such that a non-linear relationship with biophysical parameters such as the Leaf Area Index (LAI) (Baret and Guyot, 1991) is seen. The next generation of vegetation indices were developed taking into account the linearity of the cover fraction and the leaf area index, but normalizing soil brightness and color (Gilabert et al., 2011). As implied by their name, these indices refer to the soil and include the Soil Adjusted Vegetation Index (SAVI) (Huete, 1988) and the Modificied Soil Adjusted Vegetation Index (MSAVI) (Qi et al., 1994).

Other indices have been designed taking into account the spectral behavior of the soil in study areas, maintaining the sensitivity to biophysical magnitudes such as the Generalized Soil Adjusted Vegetation Index (GESAVI) (Gilabert et al., 2002). GESAVI showed good results for its linearity with LAI and soil noise reduction, simulating reflectances with radiative transfer models and with experimental data. A study by Broge and Leblanc (2001) addressing radiative transfer models has shown that the MSAVI is the best LAI estimator in terms of sensitivity-to-cover effects, variations in the cover parameters and the spectral properties of the soil. In the present work, the above vegetation indices were calculated in order to show the potential of multispectral calibrated images in agronomy.

Many studies have been carried out using multispectral and hyperspectral aerial and satellite images in the evaluation of crops (Herwitz et al., 2004; Chen et al., 2006; Zarco-Tejada et al., 2004). In fact, some authors have published works that, using multispectral, thermal or other conventional cameras on board small aircraft or unmanned helicopters, demonstrate the viability of these as platforms for image acquisition for plant studies (Esposito et al., 2007; Xiang and Tian, 2007; Turner et al., 2011; Zhao and Peng, 2006). However, to date there are no studies in which low-cost manned platforms such as PPG trikes have been used for crop monitoring. These offer an ideal platform for the study of large extensions of crops due to the above requirements.

The purpose of this article is to evaluate a new methodology aimed at acquiring georeferenced multispectral data of high spatial resolution after a radiometric calibration of the multispectral sensor for the monitoring of crops and the detection of areas with pathologies or hydric and nutritional deficiencies. To validate the methodology, a cultivated area of 5.4 ha was studied via aerial-trike overflights at different heights, using open-source software and tools. Thus, for vicarious calibration a GNU Octave (GNU, 2013) code was implemented.

The article is structured as follows: after the Introduction, Section 2 defines the method of vicarious radiometric calibration. In Section 3, the instruments used and the method developed are described. The experimental results and their discussion are given in Section 4, and the most significant conclusions are outlined in Section 5.

2. Vicarious radiometric calibration

The analysis of data captured by multispectral cameras requires prior knowledge of the radiometric calibration parameters of each channel to obtain correct interpretations. The calibration method chosen here was vicarious calibration (Dinguirard and Slater, 1999; Hernández-López et al., 2012), which involves performing an absolute radiometric calibration under flight conditions in an *in situ* radiometric measurement campaign. In this mode, the absolute method based on radiances was chosen because the digital level (DN) that defines each pixel is directly related to the radiance detected by the sensor (Hiscocks, 2011). The method based on radiances is theoretically more accurate than those based on reflectance, because it has an uncertainty of approximately only 2.8% as compared with 4.9% for the latter case (Biggar et al., 1994). This lower value is derived from the calibration and stability of the spectroradiometer required for calibration.

To carry out the radiometric adjustment, low-cost surfaces compared to other more expensive lambertian ones, have been selected as the ground control targets (invariant targets) to approximate comparable and homogenous spectral behavior under nadir observation angles to flight measurements (Davranche et al., 2009). In addition, via various laboratory tests and field studies the invariant reflective capacity for a period of time in which these surfaces were not damaged was confirmed. From the multispectral aerial images, the digital levels of these targets can be extracted and the radiance measured is obtained with the spectroradiometer on the ground, establishing a linear model for each spectral band of the sensor. To assess the effects of the atmosphere in terms of radiative transfer, the 6S Model (Vermote et al., 1997) was implemented, which transforms the radiance measured at the ground into that obtained at the height of the sensor. Finally, the results were validated with natural and artificial check targets (pseudo-invariant targets), contrasting the radiances calculated by the calibration parameters with those measured directly in the field.

Fig. 1 shows the workflow followed in the radiometric calibration process.

3. Materials and methods

3.1. Materials

The following equipment was employed for data acquisition:

- A GNSS device, Leica 1200. This consists of a RTK dual frequency receiver and geodetic GPS L2C and double dual-frequency antenna with L2C and serves to georeference control and check targets.
- A six-channel multispectral camera: Tetracam Mini-MCA. Each of the six channels of the camera is constituted by a CMOS (Complementary Metal–Oxide–Semiconductor) sensor and a filter with a preset performance against the spectral range. The spectral response of CMOS sensors is not uniform due to quantum efficiency and sensitivity. Neither do filters exhibit homogeneous transmission between each other. The effect of the combination of CMOS and the six filters results in a reduction in camera radiance, different per each wavelength. The camera specifications are defined in Table 1. The choice of the filter wavelengths (detailed in Table 2) was optimized for the evaluation of the particular behavior of the vegetation, avoiding areas of atmospheric absorption.
- A manned aerial platform supported by a powered paraglider (PPG) trike built by Airges. Its technical specifications are shown in Table 3. The Mini-MCA camera was loaded onto the PPG trike using an auto-stabilized mounting platform.
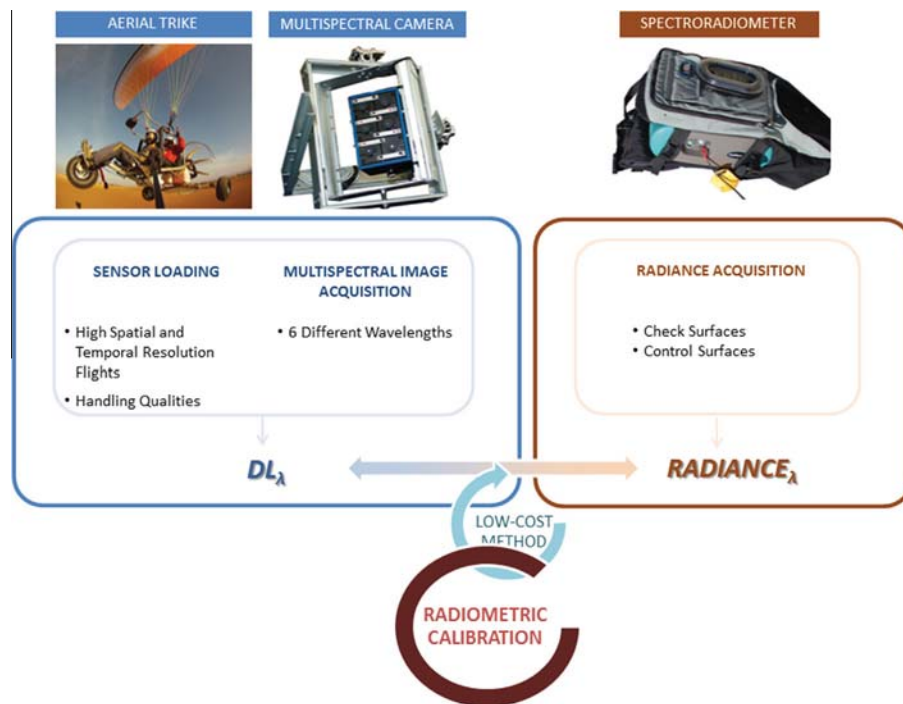
Fig. 1. Workflow of the vicarious radiometric calibration process.

Table 1
Technical specifications of the Mini-MCA multispectral camera.

Parameter	Value
Number of channels	6
Weight	700 g
Resolution	1.3 Mp per Channel
Image size	1280 × 1024 pixels
Radiometric resolution	8 bits
Capture speed	1.3 frames/s
Pixel size	5.2 μm
Focal length	9.6 mm

Table 2
Channel specifications of the Mini-MCA camera.

Channel	λmin (nm)	λmax (nm)	Exposure time (%)
0	740	820	100
1	510	550	130
2	650	690	125
3	660	740	100
4	720	760	100
5	760	840	100

Table 3
Technical specifications of the manned aerial platform, PPG trike.

Parameter	Value
Empty weight	110 kg
Maximum load	220 kg
Autonomy	3.5 h
Maximum speed	60 km/h
Motor	Rotax 503
Tandem paraglide	MACPARA Pasha 4
Emergency system	Ballistic parachutes GRS 350
Gimbal	Stabilized with 2 degrees of freedom
Minimum sink rate	1.1
Maximum glide	8.6
Plant surface	42.23 m²
Projected area	37.8 m²
Wingspan	15.03 m
Plant elongation	5.35
Central string	3.51 m
Boxes	54
Zoom factor	100%

- An aluminum multi-sensor gimbal (stabilized platform) where the multispectral camera is affixed. In particular, the gimbal includes two servomotors arranged on the x and y axes to maintain the vertical position of the camera along the flight path with precision. The servomotors are controlled by an Arduino board, which incorporates an IMU with 6 degrees of freedom: 3 accelerometers with a range of ±3.6 G m s^{-2}, a double-shaft gyroscope (for pitch and roll) and an additional gyroscope for yaw (both gyroscopes have a measurement range of ±300°/s). The software developed for the control of the device was based on Quadl_mini V 20 software, with DCM (Direction Cosine Matrix) as the management algorithm of the IMU (Premerlani and Bizard, 2013).
- A low-cost GNSS system based on a single-frequency receptor, with a signal reception of GPS constellation and SBAS (Satellite Based Augmentation System) (NavCen, 2008). The GNSS antenna is installed on the camera platform close to the optical center of the camera to minimize the baseline. In order to contrast the GNSS altitudinal accuracy that affects the final GSD, a DigiFly VL100 barometer was installed. Thus, horizontal positioning during flight was performed by the NMEA (National Marine Electronics Association) protocol of the GNSS system using RTKNAVI software (Takasu, 2009), with corrections from the ground from another similar board equipment, allowing DGPS accuracies better than 1.5 m in planimetry and 2 m in altimetry to be achieved in real time, and better than 0.5 m in 3 dimensions in postprocessing.
- A general purpose FieldSpec 3 ASD (Analytical Spectral Devices) spectroradiometer, used for the different targets (control and check) and specifically designed to acquire spectral measurements (radiance and irradiance) in the visible and near infrared ranges. The main technical specifications of the spectroradiometer are shown in Table 4.

Parameter	Value
Spectral range	350–2500 nm
Shooting time	0.1 s
Spectral resolution	1 nm
Field of view	25°

3.2. Methods

3.2.1. Flight planning and execution

The study area was located in an experimental field of the ITAP (Provincial Agricultural Technical Institute) near Albacete (Castilla La Mancha, Spain), about 21 km from the capital. Data collection was performed on the 20th of June 2013 around a vineyard, grass and a *Papaver somniferum* crop of 5.4 ha.

Proper flight planning is important to ensure that the data captured will fit the theoretical parameters pursued; it also optimizes available resources and ensures a higher quality image, minimizing capture time.

First, the study area and subsequently the plot flight paths were defined. Then, the flight planning process defined the position and orientation of the camera, the design of different blocks of images, determination of the overlaps between different images, the necessary shot angles and guarantee of the scale through choice of the pixel size on the ground (GSD). A GSD of 0.08 m and 0.15 m was selected in this study.

The geomatic information required for the flight planning process can be obtained freely from the National Center of Geographic Information in Spain (CNIG), from its National Aerial Orthoimage Plan (PNOA, 2009) with a GSD of 0.25 m and a Digital Terrain Model (DTM) with a 5-m grid resolution.

Flight planning was performed by considering the relationship between flight altitude over the ground (H), the GSD, the focal length of the sensor (f) and pixel size, as described in Eq. (1).

$$\frac{f}{H} = \frac{pixel\,size}{GSD} \tag{1}$$

Considering Eq. (1), the characteristics of the camera (Table 1) and the required GSD of 0.08 m and 0.15 m, flight altitudes over the ground of 145 m and 245 m are obtained respectively. Also, additional restrictions, such as a minimum forward overlap of 60% and a minimum side overlap of 20% were established. The flight planning obtained is outlined in Fig. 2, where rectangles are the areas capture by each image shot in the point position.

3.2.2. Field data acquisition

In the study area, control and check targets were selected and positioned (Fig. 3) taking the GSD dimension into account.

The control and check targets used in the data collection are specified for both flights in Table 5.

In the radiometric campaign, calibration targets were characterized by the spectroradiometer as radiant flux detector. During data acquisition, the angle between the gun of the spectroradiometer and the targets measured was kept as orthogonal as possible, taking two measurements with an average of 30 spectral measurements per cover. In order to avoid the BRDF effects, the tarps have been characterized at field with enough number of samples to reject spectral reflectance anomalies.

Figs. 4 and 5 show the spectral signatures of the colored and grayscale tarps acquired in the radiometric campaign. The reflectance of these targets was obtained as the ratio of the reflected radiance of each cover and the irradiance provided by a reference target (Spectralon® 99%), both measured with the spectroradiometer.

At the same time, and in order to avoid significant atmospheric variations, a planned PPG trike flight was conducted over the study area with a 0.08 m GSD (at 145 m height) and 0.15 m GSD (at 245 m height), capturing multispectral images (Fig. 6) and finally choosing those in which the maximum number of control and check targets appeared.

3.3. Calibration methodology and fitting model

Measured radiance serves as ground truth, establishing a connection with the digital level of the corresponding wavelength. On one hand, radiance was measured in a spectral range of 350–2500 nm with a nanometer resolution. On the other, the Mini-MCA recorded digital levels in its 6 channels, characterized by the response of the filters and CMOS per wavelength. Thus, the radiometric measurements were resampled and standardized for the spectral resolution of the camera.

In addition, digital levels were corrected for vignetting and the systematic background noise produced by each lens (Kelcey and Lucieer, 2012). The vignetting study was performed at the laboratory with uniform lighting, capturing images of a white pattern with low specular reflection (Zheng et al., 2009). The systematic background noise was evaluated at the laboratory under the absence of lighting conditions and analyzing the average response of the camera per channel for its different exposure times.

Because there are several images involved in calibration adjustment, a homogenization factor of luminance between images was taken into account to neutralize the exposure differences. These differences are caused by changes in lighting between different image captures and the exposure time of each channel, according

Fig. 2. Flight planning of 0.15 m GSD (at 245 m height) (a) and 0.08 m GSD (at 145 m height) (b).
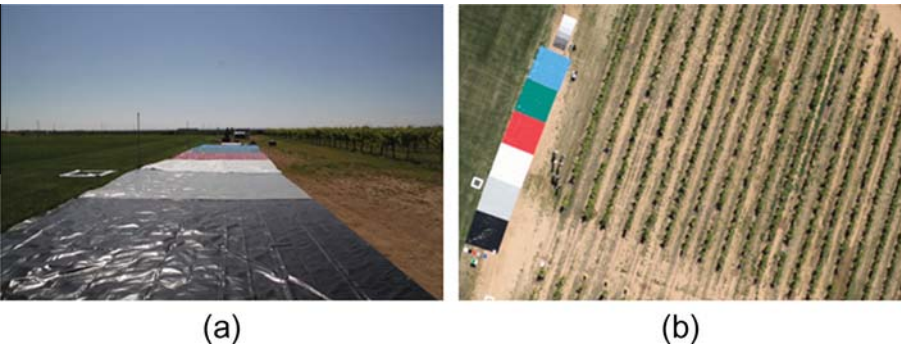
Fig. 3. Terrestrial image of the control targets for the radiometric calibration (a) aerial image of the calibration targets and study area (b).

Table 5
Description of the control and check PCV targets.

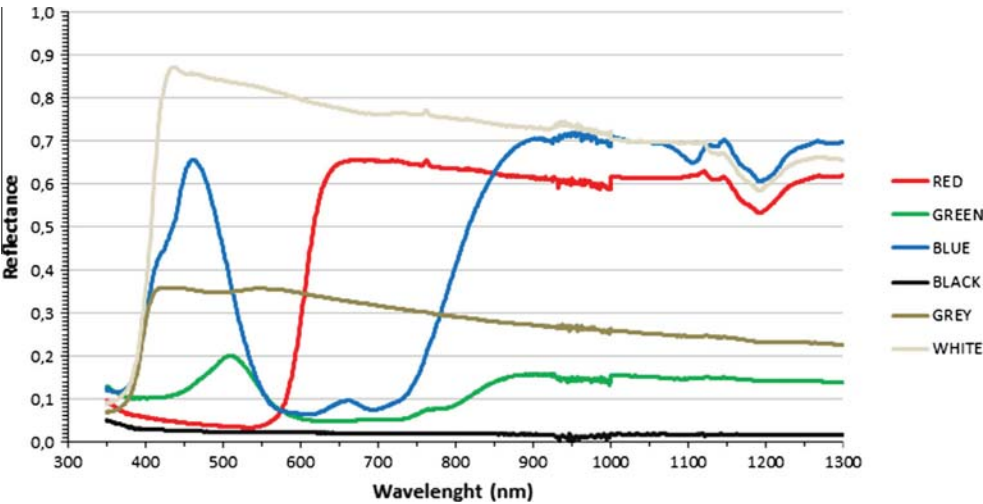| Control	Type	Material	Size	Color
		PVC tarp	5 m × 1 m	Grayscale (5 steps)
Control targets	Artificial	PVC tarp	5 m × 1 m	Black Gray White Red Green Blue
Check targets	Artificial	PVC surface	0.55 m × 0.35 m	Black Gray White Red Green Blue
		Brown wrapping paper Cork Cardboard Grass Ground		
	Natural	Grapevine *Papaver somniferum*		

Fig. 4. Spectral signature from 350 nm to 1300 nm of the control targets (PVC tarps) obtained in the field with the spectroradiometer.

to the manufacturer. This factor corrects digital levels and depends on the channel and the image. Also, a common unknown per image and invariant for each channel was included in order to absorb possible discrepancies between the standard and real atmosphere for each image.

The mathematical model used is shown in the following figure (Fig. 7), where X is the vector of calibration coefficients (unknowns); A is the design matrix (corrected digital levels of control targets in the images) and L is the vector of independent terms (radiance measures of control targets).

Eq. (2) summarizes this model:

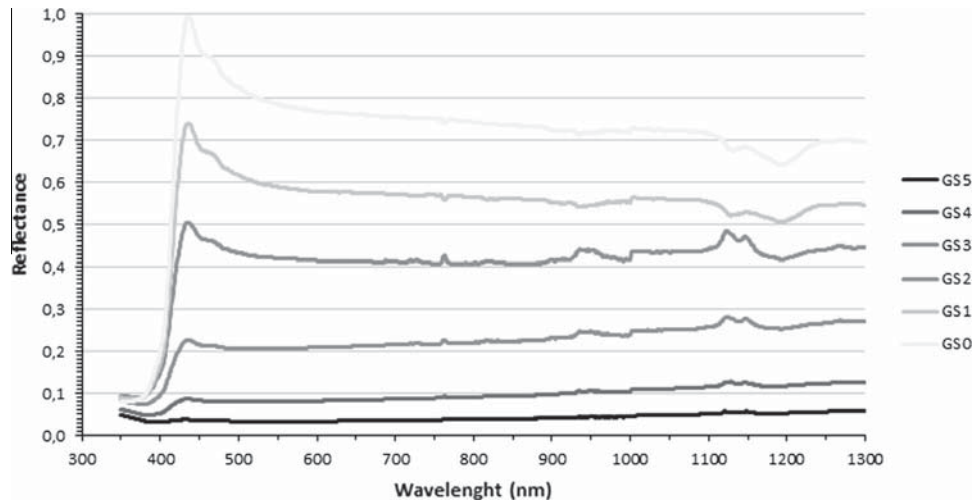$$L = F_0 + F_1 \cdot DN_c, \tag{2}$$

where

Fig. 5. Spectral signature from 350 nm to 1300 nm of the control targets (Grayscale tarp) obtained in the field with the spectroradiometer.
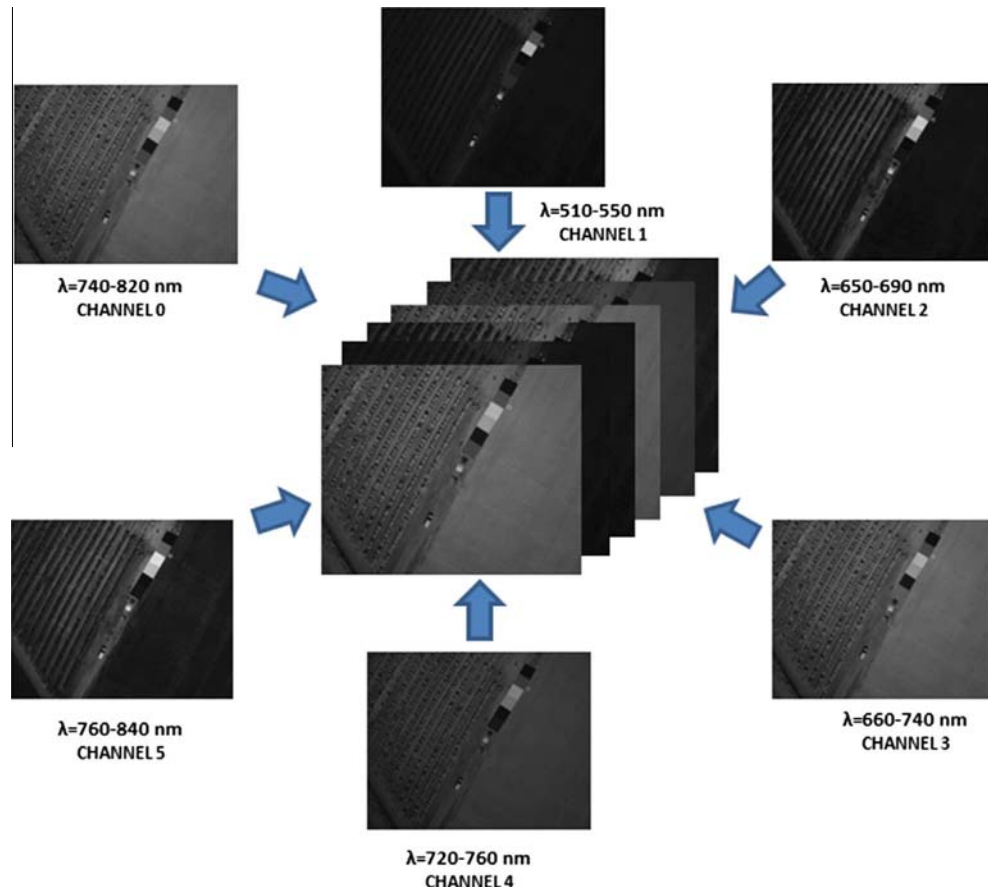

Fig. 6. Multispectral images used in the radiometric calibration process.

L is the measured radiance of each control target,
DN_c is the digital level of control targets corrected by luminance, vignetting and the systematic background noise,
F_0 is the offset calibration coefficient of each channel,
F_1 is the gain calibration coefficient of each channel.

The unknowns are obtained by solving the over-determined system without rank default, performing a robust estimation with the Danish Method (Krarup et al., 1980), which rejects the out-of-range observations (outliers), giving a series of weights based on the residual values obtained in the previous iteration.

3.4. Atmospheric correction

In aerial radiometry, the aim is to determine physical values at ground level. In this way, an atmospheric model must be applied to study the behavior of radiance propagation because of scattering and absorption processes (Hernández-López et al., 2011). In this study case, the 6S radiative transfer model (Vermote et al., 1997) was applied for the less favorable flight (0.15 m GSD flight at 245 m height).

With regard to atmospheric parameters, the values of aerosol optical depth (AOD) were taken from AERONET (aerosol robotic
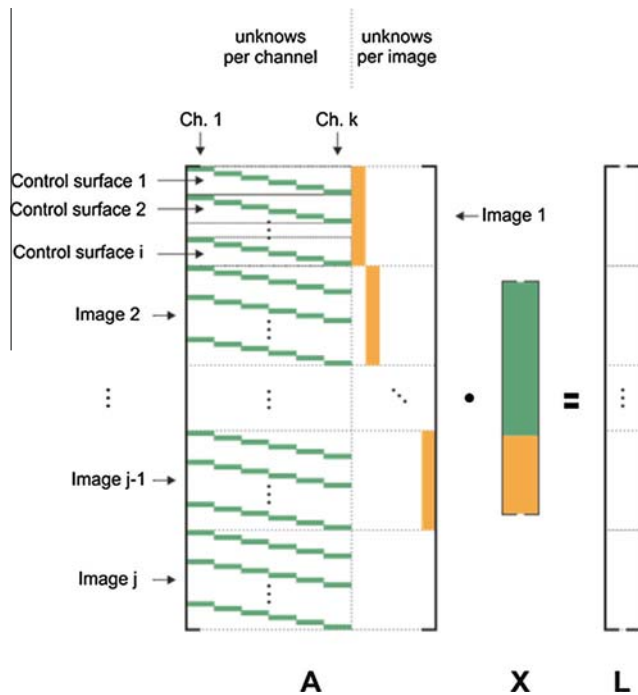
Fig. 7. Mathematical model of the radiometric calibration process.

network). Owing to the absence of closer stations, the AOD value was extracted as the average of the values of two closest stations, approximately 200 km from Albacete in the North-West and South-East directions (Madrid and Burjassot, respectively).

For each control target, sun direction was obtained at the moment of image acquisition, expressed by the geodetic azimuth and the zenith angle from the vertical. For this calculation, the Solar Position Algorithm (SPA) library (Reda and Andreas, 2004) was used. The input parameters were obtained from known flight data and GNSS measurements. Once solar direction had been calculated, the atmospheric parameters were obtained from the 6S Model, which creates an atmospheric profile on the control targets involved in the calibration process for each of the channels. Among the atmospheric parameters calculated, irradiance per image and channel and radiance and reflectance at ground and sensor per target and channel were included.

According to the data obtained, the relative influence of the atmosphere is minimal because the atmospheric column spanned by the radiation is unimportant and can be neglected in the calculations, demonstrating that sensor radiances at 1 m or 245 m height (using 6S model (Vermote et al., 1997)) were fairly similar to those measured at ground level with the spectroradiometer.

3.5. Derived geomatic products

Geomatic products are characterized by their spatial, spectral, radiometric and temporal resolution (Aber et al., 2010). In the present case, spatial resolution was limited by a GSD of 0.15 m, considered sufficient for this type of agricultural study. Temporal resolution was established considering the phenological aspects of the crop and environmental aspects. Regarding spectral resolution, this is limited to the band width of the six filters chosen to detect certain types of plant behavior in the most appropriate spectrum, avoiding areas of atmospheric absorption.

Advances in computer vision, photogrammetry and new low-cost GNSS and IMU systems make it possible to obtain orthoimages generated from images captured with a non-metric digital camera aboard a low-cost aerial platform (Aber et al., 2010).

Finally, images were georeferenced considering Coordinate Reference System (CRS) ETRS89 UTM 30 (EPSG code 25830), which is required by Spanish legislation in all geomatic products. In the navigation phase, which uses a GNNS, WGS84 CRS was employed (EPSG code 4326).

4. Experimental results and discussion

Below, the calibration parameters of the Mini-MCA camera are reported. F_0 is the offset coefficient and F_1 is the gain coefficient (Tables 6 and 7) obtained for each of the six channels achieved in the mathematical fitting of the two flights with different GSD. The *a posteriori* variance in unit weight shows a value of 0.0043 W m^{-2} sr^{-1} and a correlation coefficient of adjustment, R^2, of 0.9940.

In both flights, the detection of outliers was studied in order to avoid outliers. Standardized errors were calculated with the Pope Statistical Test (Pope, 1976), the maximum standardized residual of 2.800 remaining under the threshold of 3.916 established at the 95% of confidence level with a Tau distribution.

Together with the detection of outliers, internal fiability was tested by means of redundancy number analysis. As a result, all the equations contribute to approximately the same extent, without there being an increased presence of certain observations, due to the internal design of the proposed system, confirming the absence of outliers in the observations. The redundancy numbers of the adjustment entail a range between 0.9306 and 0.9995 for both flights.

A statistical analysis of the resulting coefficients for both flights was performed in order to assess their differences. The statistical parameter was defined as:

$$Z = \frac{\mu_1 - \mu_2}{\sqrt{\sigma_{\mu_1}^2 + \sigma_{\mu_2}^2}} \tag{3}$$

where $\sigma_{\mu 1}$ is the standard error of the mean value calculated as:

$$\sigma_{\mu_1} = \frac{\sigma}{\sqrt{n}} \tag{4}$$

The critical value for a two-tailed test at 5% of significance is ±1.96 using a normal distribution. According to the results shown in Table 8, the resulting coefficients of both flights show no significant differences, so the null hypothesis of both samples belonging to the same distribution can be accepted.

Table 6
Radiometric calibration coefficients of the multispectral camera for 0.08 m GSD flight (at 145 m height) in radiance units (W m^{-2} sr^{-1}).

Channel	F_0 value	F_1 value
0	−60.5584	2627.3057
1	19.2122	4002.9353
2	2.7057	3108.6876
3	−13.0825	2590.2099
4	−84.4579	4349.9835
5	−60.9567	2660.1684

Table 7
Radiometric calibration coefficients of the multispectral camera for 0.15 m GSD flight (at 245 m height) in radiance units (W m^{-2} sr^{-1}).

Channel	F_0 value	F_1 value
0	−77.1444	2548.2911
1	15.6807	3798.3712
2	−16.4305	2930.0517
3	−20.3672	2428.5566
4	−89.7453	4250.6229
5	−67.3736	2947.6022

Table 8
Statistical comparison of the radiometric calibration coefficients of both flights.

Channel	F_0		F_1	
	Z score	P value	Z score	P value
0	0.0143	0.9886	0.0399	0.9682
1	0.0033	0.9974	0.0979	0.9220
2	0.0167	0.9866	0.0922	0.9265
3	0.0066	0.9948	0.0886	0.9294
4	0.0046	0.9963	0.0406	0.9676
5	0.0055	0.9956	−0.1341	0.8933

To address statistical significance, two complementary hypotheses were established. In this case, H_0 establishes that residual values are distributed according to a normal distribution with mean zero, whereas H_a considers that the distribution mean is a nonzero value. The F_0 and F_1 parameters were studied in both flights, obtaining p-values greater than 0.279 and less than 0.001 respectively. Working with a 95% confidence interval, the F_0 coefficient may be negligible but not the F_1 coefficient. This is in agreement with the specifications of the manufacturer in that the offset parameter is negligible. To validate the results, the mean of the absolute values of the residuals per channel of the targets (control and check targets) between the measured and calculated radiance was used. This parameter was always below $0.01\ \mathrm{W\,m^{-2}\,sr^{-1}}$ (Table 9).

Because the residuals in the 0.08 m GSD flight were lower than in the 0.15 m GSD flight, the parameters at 0.08 m GSD flight were analyzed in order to be used in future studies. Fig. 8 shows a representation of the mean radiance errors of the different control targets per channel used in the calibration process.

A statistical study was conducted to check the calibration process Table 10 shows the statistical parameters of errors (Eq. (5)) calculated as differences between ground radiance measurement with the spectroradiometer on check targets and radiance calculated by digital levels and the parameters resulting from the calibration process (Eq. (6)).

$$v = L_{measured} - L_{calculated} \tag{5}$$

$$L_{calculated} = F_0 + F_1 \cdot DNc \tag{6}$$

where

v: check target error,
$L_{measured}$: check target measured radiance,
$L_{calculated}$: check target calculated radiance,
DN_c: digital level corrected by variations in exposure time between channels, vignetting and systematic background noise,
F_0: offset calibration coefficient from each camera channel,
F_1: gain calibration coefficient from each camera channel.

The standard deviation (σ) (Eq. (7)), root mean square error (*rm*se) (Eq. (8)) and average error $|\vec{v}|$ in absolute values (Eq. (9)) are shown in Table 10, and are defined as follow:

$$\sigma = \sqrt{\frac{1}{n-1}\sum_{i=1}^{n}(v_i - \bar{v})^2} \tag{7}$$

$$rmse = \sqrt{\frac{1}{n}\sum_{i=1}^{n}(v_i)^2} \tag{8}$$

$$|\vec{v}| = \frac{\sum_{i=1}^{n}|v_i|}{n} \tag{9}$$

This shows that most of the check targets, assumed to be pseudo-invariant targets, are suitable for the validation of radiometric calibration. In general, artificially colored uniform surfaces, such as PVC targets, provided the best precision in the six channels

Table 9
Mean of the absolute values of the residuals per channel in $\mathrm{W\,cm^{-2}\,sr^{-1}}$.

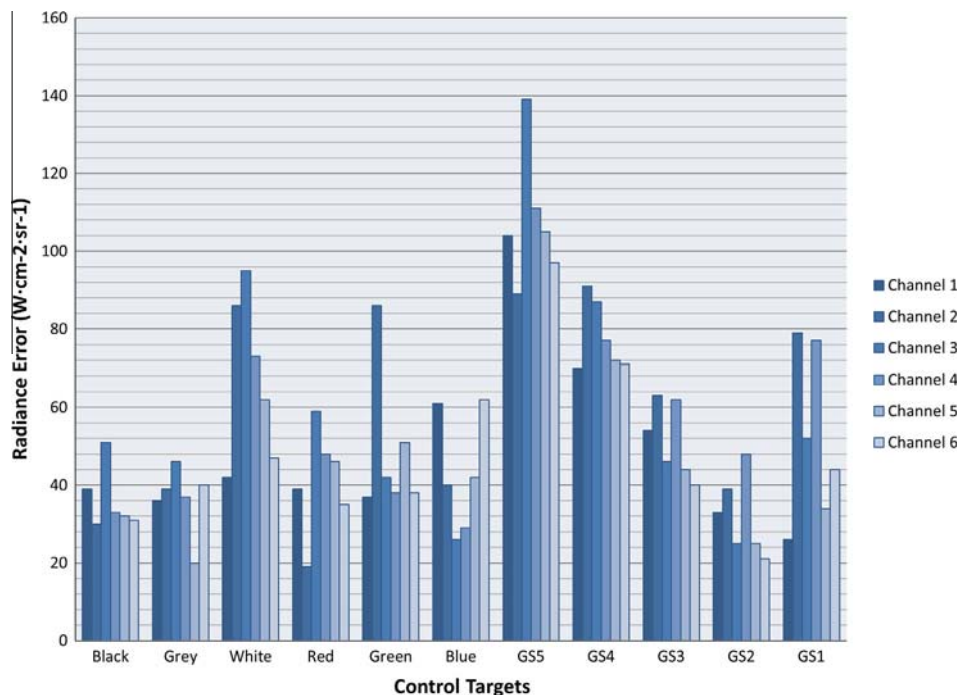| Flight GSD(m)/height(m)	Ch. 0	Ch. 1	Ch. 2	Ch. 3	Ch. 4	Ch. 5
0.08/145	36.22	43.71	42.77	35.82	37.32	31.46
0.15/245	45.32	66.29	53.46	52.07	47.41	54.88

Fig. 8. Mean of the radiance errors of the different control targets ($\mathrm{W\,m^{-2}\,sr^{-1}}$) per channel.

Table 10
Statistical values of errors in the vicarious calibration performed on different check targets expressed in radiances (W m^{-2} sr^{-1}), where σ is the standard deviation, *rmse* is the root mean square error, and $|\bar{v}|$ is the average absolute error value.

Target	Statistical parameter	Channel 0	Channel 1	Channel 2	Channel 3	Channel 4	Channel 5
Blue PVC	σ	61.33	54.88	17.00	33.03	44.62	63.75
	rmse	68.49	47.77	86.02	140.20	74.55	55.22
	$|\bar{v}|$	43.25	43.25	84.75	137.25	63.75	45.00
Gray PVC	σ	181.10	80.38	87.59	68.52	93.27	42.43
	rmse	158.47	417.84	272.76	140.18	104.63	37.41
	$|\bar{v}|$	124.25	412.00	262.00	127.00	103.00	33.00
Green PVC	σ	49.11	59.61	80.64	46.12	68.77	43.07
	rmse	151.11	189.90	137.55	140.78	151.22	177.71
	$|\bar{v}|$	145.00	182.75	118.50	135.00	139.00	173.75
Red PVC	σ	146.71	20.94	144.03	112.53	198.00	111.80
	rmse	270.67	42.56	588.37	352.01	350.12	225.13
	$|\bar{v}|$	239.00	38.50	575.00	338.25	305.25	203.25
Black PVC	σ	15.41	37.10	18.63	41.84	38.20	28.52
	rmse	167.51	222.40	211.18	186.09	180.31	157.67
	$|\bar{v}|$	167.50	222.38	211.18	186.05	180.28	157.65
White PVC	σ	214.36	133.39	195.42	209.22	230.73	167.65
	rmse	560.86	1492.48	1063.80	666.12	590.34	491.68
	$|\bar{v}|$	529.25	1488.00	1050.25	641.00	555.50	469.75
Ground	σ	9.90	11.31	7.07	24.75	28.99	12.02
	rmse	99.25	149.21	287.04	95.12	113.37	42.36
	$|\bar{v}|$	99.00	149.00	287.00	93.50	111.50	41.50
Brown Wrapping Paper	σ	58.94	84.68	81.93	103.23	111.70	101.10
	rmse	51.27	73.98	153.66	94.62	96.43	89.79
	$|\bar{v}|$	47.67	63.00	138.33	80.33	87.33	86.67
Cardboard	σ	57.14	52.00	73.60	138.30	88.06	93.22
	rmse	436.17	591.19	731.14	466.21	421.84	351.67
	$|\bar{v}|$	−433.67	−589.67	−728.67	−452.33	−415.67	−343.33
Grass	σ	141.20	69.85	48.06	54.24	100.34	112.49
	rmse	129.85	102.45	58.18	63.52	90.71	112.71
	$|\bar{v}|$	127.40	81.20	42.40	44.20	75.60	106.80
Grapevine	σ	–	–	–	–	–	–
	rmse	169.00	59.00	42.00	22.00	294.00	128.00
	$|\bar{v}|$	169.00	59.00	42.00	22.00	294.00	128.00
Cork	σ	14.14	26.16	72.12	65.05	91.22	29.70
	rmse	417.12	330.02	629.07	473.24	416.52	384.57
	$|\bar{v}|$	417.00	329.50	627.00	471.00	411.50	384.00
P. somniferum.	σ	–	–	–	–	–	–
	rmse	469.00	185.00	355.00	225.00	334.00	345.00
	$|\bar{v}|$	469.00	185.00	355.00	225.00	334.00	345.00

of the spectrum, while more heterogeneous surfaces such as the ground or vegetation afforded poorer results. These are anisotropic and less homogeneous surfaces than PVC, with higher variations in the radiance leaving the target and its reflectance. This produces a slight increase in its *rmse* and σ.

All these results confirm the feasibility of using tarps of different colors as a low-cost alternative to spectralon with certain limitations for vicarious radiometric calibration. As a result, several measurements can be obtained by increasing the number of targets and hence improving the quality of the mathematical fitting.

Although not aiming to investigate the performance of the different vegetation indices, an example of the product generated using the georeferenced multispectral reflectance images is provided in this work in order to highlight its potential in agricultural studies. Four multispectral vegetation indices were selected taking into account that they are widely applied in agronomy owing to their sensitivity to vegetation and their normalization of soil background brightness and color: NDVI, SAVI, MSAVI and GESAVI. The latter was parameterized for the soil characteristics in the study area.

These images were processed with algorithms defined in the 2nd and 5th channel of the multispectral sensor (670 and 800 nm) (Fig. 8) through an implemented code in GNU Octave software.

The reflectance of each pixel was obtained from the calculated radiance and irradiance per channel acquired previously with a calibrated PVC target that appeared on the image, according to Eq. (10) for each sensor channel [24], under the assumption of a Lambertian surface.

$$\rho = \frac{L_{calculated} \cdot \pi}{E} \tag{10}$$

where $L_{calculated}$ is the radiance calculated from each target and E is the irradiance per channel.

Although the indices addressed here do not have the same range of variation, all of them identify the plant trellis in the scene, as can be seen in Fig. 9. They enhance the photosynthetic activity in the scene, showing not only the presence of the vineyard plants but also other small plants between the rows. The darkest areas correspond to non-vegetated areas. These images can also be compared quantitatively to other flight dates allowing the vineyard to be monitored for the managing of nutrients, diseases or water supply within the plot.
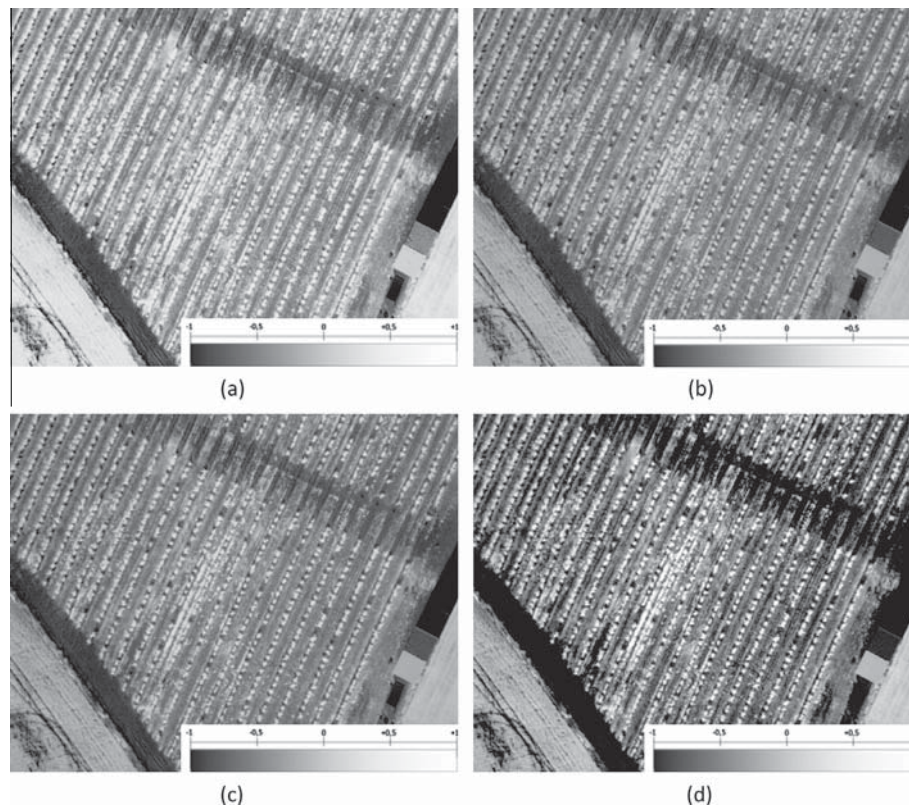
Fig. 9. Different plant indices in the vineyard area derived from the radiometric calibration: (a) NDVI Image, (b) SAVI Image, (c) MSAVI Image and (d) GESAVI Image.

5. Conclusions

This paper describes a successful methodology for radiometric calibration using the vicarious method of a multispectral Mini-MCA camera aboard a low-cost manned aerial platform and using low-cost targets of invariant reflectivity material. The statical analysis of the errors confirms the validity of the method. For this purpose, a flight at two different heights was carried out to test adjustment stability, the calibration coefficients being statistically consistent in both cases, demonstrating insignificant relative atmospheric effects occurring in flights below 300 m on a clear and sunny day. In fact, this is the maximum height at which these platforms are permitted to fly according to Spanish legal constraints. The results confirm a new trend for low-cost remote sensing, together with the use of the latest computer vision techniques and open-source geomatic tools. In this study case, the calibrated geomatic products can be used to successfully evaluate and classify large areas of different crops, allowing decisions to be made about irrigation, nutritional support and crop development through accurate georeferenced and calibrated multispectral images. Compared to classic aerial photogrammetric platforms (aircraft), the proposed methodology cuts costs. Regarding satellite systems, their temporal and spatial resolution generates a major limitation in applications to crops. The potential of this PPG trike system is evident, with the possibility of being able to load it with a large number of sensors that extend multispectral studies, affording the advantage of a flying height that minimizes the need for atmospheric corrections. Here, the potential of deriving quantitative magnitudes such as vegetation indices is also shown. Future works will address the assimilation of the calibrated images into agronomic models to evaluate their consistency with advanced biophysical variables.

References

Aber, J.S., Marzolff, I., Ries, J., 2010. Small-Format Aerial Photography: Principles, Techniques and Geoscience Applications. Elsevier Science, The Netherlands.

Baret, F., Guyot, G., 1991. Potentials and limits of vegetation indices for LAI and APAR assessment. Remote Sens. Environ. 35, 161–173.

Berni, J., Zarco-Tejada, P.J., Suarez, L., Fereres, E., 2009. Thermal and narrowband multispectral remote sensing for vegetation monitoring from an unmanned aerial vehicle. IEEE Trans. Geosci. Remote Sens. 47 (3), 722–738.

Biggar, S.F., Slater, P.N., Gellman, D.I., 1994. Uncertainties in the in-flight calibration of sensors with reference to measured ground sites in the 0.4–1.1 μm range. Remote Sens. Environ. 48 (2), 245–252.

Biggar, S.F., Thome, K.J., Wisniewski, W., 2003. Vicarious radiometric calibration of EO-1 sensors by reference to high-reflectance ground targets. Geosci. Remote Sens., IEEE Trans. 41 (6), 1174–1179.

Broge, N.H., Leblanc, E., 2001. Comparing prediction power and stability of broadband and hyperspectral vegetation indices for estimation of green leaf area index and canopy chlorophyll density. Remote Sens. Environ. 76 (2), 156–172.

Chen, X., Zhao, H., Li, P., Yin, Z., 2006. Remote sensing image-based analysis of the relationship between urban heat island and land use/cover changes. Remote Sens. Environ. 104 (2), 133–146.

Chuvieco, E., Huete, A., 2009. Fundamentals of Satellite Remote Sensing. CRC Press Inc.

Davranche, A., Lefebvre, G., Poulin, B., 2009. Radiometric normalization of SPOT-5 scenes: 6S atmospheric model versus pseudo-invariant features. Photogramm. Eng. Remote Sens. 75 (6).

Dinguirard, M., Slater, P.N., 1999. Calibration of space-multispectral imaging sensors: a review. Remote Sens. Environ. 68 (3), 194–205.

Esposito, F., Rufino, G., Moccia, A., 2007. 1st Mini-UAV Integrated Hyperspectral/Thermal Electro-Optical Payload for Forest Fire Risk Management. In: Proc. AIAA InfotechAerosp. Conf. pp. 653–665.

Gilabert, M.A., González-Piqueras, J., García-Haro, F.J., Meliá, J., 2002. A generalized soil-adjusted vegetation index. Remote Sens. Environ. 82, 303–310.

Gilabert, M.A., González-Piqueras, J., Martínez, B., 2011. Theory and application of vegetation indices. In: Maselli, F., Menentiani, M., Brivio, P.A. (Eds.), Optical Observation of Vegetation Properties and Characteristics. Research Signpost, Kerala, India, pp. 1–43.

http://www.gnu.org/software/octave (accessed 01.12.13).

Hailey, T.I., 2005. The powered parachute as an archaeological aerial reconnaissance vehicle. Archaeol. Prospection 12 (2), 69–78.

Hernández-López, D., Felipe-García, B., González-Piqueras, J., Alcázar, G.V., 2011. An approach to the radiometric aerotriangulation of photogrammetric images. ISPRS J. Photogramm. Remote Sens. 66 (6), 883–893.

Hernández-López, D., Felipe-García, B., Sánchez, N., González-Aguilera, D., Gomez-Lahoz, J., 2012. Testing the radiometric performance of digital photogrammetric images: vicarious vs. laboratory calibration on the Leica ADS40, a study in Spain. Photogramm. Fernerkundung Geoinform. 2012 (5), 557–571.

Hernandez-Lopez, D., Felipe-Garcia, B., Gonzalez-Aguilera, D., Arias-Perez, B., 2013. An automatic approach to UAV flight planning and control for photogrammetric applications: a test case in the asturias region (Spain). Photogramm. Eng. Remote Sens. 79 (1), 87–98.

Herwitz, S.R., Johnson, L.F., Dunagan, S.E., Higgins, R.G., Sullivan, D.V., Zheng, J., Lobitz, B.M., Leung, J.G., Gallmeyer, B.A., Aoyagi, M., Slye, R.E., Brass, J.A., 2004. Imaging from an unmanned aerial vehicle: agricultural surveillance and decision support. Comput. Electron. Agric. 44, 49–61.

Hiscocks, P.D., 2011. Measuring Luminance with a Digital Camera. <http://www.ee.ryerson.ca/~phiscock/astronomy/light-pollution/luminance-notes.pdf> (accessed 17. 07. 14).

Honkavaara, E., Arbiol, R., Markelin, L., Martinez, L., Cramer, M., Bovet, S., Chandelier, L., Ilves, R., Klonus, S., Marshal, P., Schläpfer, D., Tabor, M., Thom, C., Veje, N., 2009. Digital airborne photogrammetry—a new tool for quantitative remote sensing?—a state-of-the-art review on radiometric aspects of digital photogrammetric images. Remote Sens. 1 (3), 577–605.

Huete, A.R., 1988. A soil-adjusted vegetation index. Remote Sens. Environ. 25, 298–309.

Kelcey, J., Lucieer, A., 2012. Sensor correction of a 6-band multispectral imaging sensor for UAV remote sensing. Remote Sens. 4, 1462–1493.

Krarup, T., Juhl, J., Kubik, K., 1980. In: Götterdammerung Over Least Squares Adjustment, XIV Congress of International Society of Photogrammetry, Hamburg; Hamburg. pp. 369–378.

Lass, L.W., Callihan, R.H., 1997. The effect of phenological stage on detectability of yellow hawkweed (Hieraciumpratense) and oxeye daisy (Chrysanthemum leucanthemum) with remote multispectral digital imagery. Weed Technol. 11 (2), 248–256.

NavCen, 2008. Global Positioning System Standard Positioning Service Performance Standar, 4th ed. US Department of Defense: Position, Navigation, and Timing Executive Committee, Washington, DC.

Pope, A.J. 1976. The statistics of residuals and the detection of outliers. In: NOAA Technical Report NOS 65 NGS 1, National Ocean Service, National Geodetic Survey. US Department of Commerce, Rockville, MD, Washington, 133pp.

Premerlani, W., Bizard, P., 2013. Direction Cosine Matrix IMU: Theory. <http://gentlenav.googlecode.com/files/DCMDraft2.pdf> (accessed 01.12.13).

Qi, J., Chehbouni, A., Huete, A., Kerr, Y., Sorooshian, S., 1994. A modified soil adjusted vegetation index. Remote Sens. Environ. 48 (2), 119–126.

Reda, I., Andreas, A., 2004. Solar position algorithm for solar radiation applications. Sol. Energy 76 (5), 577–589.

Rouse, J.W., Haas, R.H., Schell, J.A., Deering, D.W., Harlan, J.C., 1974. Monitoring the vernal advancement of retrogradation of natural vegetation, NASA/GSFC, Type III. In: Final Report. Greenbelt, MD, p. 371.

Schmidt, K.S., Skidmore, A.K., 2003. Spectral discrimination of vegetation types in a coastal wetland. Remote Sens. Environ. 85 (1), 92–108.

Takasu, T., 2009. RTKLIB: Open Source Program Package for RTK-GPS. FOSS4G, Tokyo, Japan.

Turner, D., Lucieer, A., Watson, C., 2011. Development of an Unmanned Aerial Vehicle (UAV) for hyper resolution vineyard mapping based on visible, multispectral, and thermal imagery. In: Proceedings of 34th International Symposium on Remote Sensing of Environment. p. 4.

Vermote, E.F., Tanre, D., Deuze, J.L., Herman, M., Morcette, J.J., 1997. Second simulation of the satellite signal in the solar spectrum, 6S: an overview. IEEE Trans. Geosci. Remote Sens. 35 (3), 675–686.

Xiang, H., Tian, L., 2007. Autonomous Aerial Image Georeferencing for an UAV-Based Data Collection Platform Using Integrated Navigation System. ASABE Annual Meeting, Minneapolis, Minnesota.

Zarco-Tejada, P.J., Miller, J., Morales, A., Berjón, A., Agüera, J., 2004. Hyperspectral indices and model simulation for chlorophyll estimation in open-canopy tree crops. Remote Sens. Environ. 90 (4), 463–476.

Zhang, C., Kovacs, J., 2012. The application of small unmanned aerial systems for precision agriculture: a review. Precision Agric. 13 (6), 693–712.

Zhao, W.T., Peng, J.Y., 2006. VORONOI diagram-based path planning for UAVs. J. Syst. Simul. 18 (2), 159–162.

Zheng, Y., Lin, S., Kambhamettu, C., Jingyi, Y., Sing Bing, K., 2009. Single-image vignetting correction. IEEE Trans. Pattern Anal. Mach. Intell. 31, 2243–2256.